Mechanism of breakaway oxidation of Fe–Cr and Fe–Cr–Ni alloys in dry and wet carbon dioxide

Thomas Gheno, Daniel Monceau, David Young

Mechanism of breakaway oxidation of Fe–Cr and Fe–Cr–Ni alloys in dry and wet carbon dioxide

Thomas Gheno[1,2], Daniel Monceau[1] and David J. Young[2]*

[1] *Institut Carnot CIRIMAT, ENSIACET, 31030 Toulouse Cedex 4, France*
[2] *School of Materials Science and Engineering, The University of New South Wales, Sydney, NSW 2052, Australia*

This is the accepted version of an article published in Corrosion Science, available at:
https://doi.org/10.1016/j.corsci.2012.07.024

Abstract. Model Fe–Cr and Fe–Cr–Ni alloys were exposed to Ar–CO_2 and Ar–CO_2–H_2O gas mixtures at 650 °C. While all alloys initially formed protective Cr_2O_3 scales, nucleation and growth of iron-rich oxide nodules resulted in some cases in breakaway oxidation. The conditions leading to departure from the protective stage are discussed in terms of Cr_2O_3 thermodynamic and kinetic stability. The morphological and compositional evolutions accompanying nodule development were examined. The influence of carbide precipitation on alloy chromium diffusion and the ability of the alloy to form and maintain Cr-rich oxide layers was investigated.

Keywords: Steel; High temperature corrosion; Internal oxidation; Selective oxidation

1 Introduction

As part of the global effort to mitigate carbon dioxide emissions from coal-fired power plants, oxy-fuel combustion has emerged as a promising alternative to conventional technologies. As nitrogen is eliminated from the inlet gas, and coal is burnt in a mixture of oxygen and recirculated flue gas, the exhaust gas contains mainly CO_2 and H_2O, allowing easier separation of CO_2 for sequestration. The changed gas composition raises the question of fireside corrosion resistance of structural alloys in CO_2 + H_2O-rich atmospheres [1].

Ferritic and austenitic chromium-containing steels are used for various heat-resisting applications at moderate temperatures. However, Fe–Cr alloys are particularly prone to breakaway oxidation, defined as a rapid acceleration of the reaction rate. Breakaway is associated with the rapid growth of Fe-rich oxides on alloys initially forming protective Cr-rich oxide scales.

Commercial and model Fe–Cr materials which oxidise protectively in air have been shown to suffer breakaway oxidation in CO_2 [2–4]. The deleterious effect of CO_2 was related [2] to the extensive internal precipitation of chromium-rich carbides, which hinders the outward diffusion and selective oxidation of chromium.

Similarly, the addition of H_2O to a gas mixture, or its substitution for oxygen, is known to trigger breakaway oxidation of Fe–Cr alloys [5–9]. Various explanations of this effect have been proposed. Chromia scales have been shown to grow faster

*Corresponding author. Tel.: +61 2 9385 4322; fax: +61 2 9385 5956.
E-mail address: d.young@unsw.edu.au (D.J. Young).

Table 1: Alloy composition (wt. %, base = Fe) and phase constitution (as annealed, determined by XRD).

Cr	Ni	
20		α
20	10	γ–α
20	20	γ
25		α
25	10	γ–α
25	20	γ

in the presence of H_2O [9–12], which has been attributed to hydrogen dissolution (in the form of OH^-) in the oxide [13]. The dissolution of hydrogen in the metal matrix is suggested to enhance internal oxidation of chromium, by increasing the permeability of oxygen [14]. In the presence of both oxygen and water vapour at moderate temperatures, formation of volatile species from Cr_2O_3 has been shown to enhance chromium depletion and trigger breakaway [4,15,16].

Recent studies [3,4] indicated that exposure of Fe–Cr alloys to CO_2–H_2O produced results similar to those observed in CO_2 or H_2O. The minimum chromium concentration required for Cr_2O_3 formation is increased by about the same amount in these atmospheres, over that required in air. The influence of alloy chromium concentration on the thermodynamic and kinetic stability of Cr_2O_3 has been studied [17,18], but a detailed description of the effect of CO_2 and H_2O is lacking. Furthermore, while the oxide morphology developed during the steady-state stage of non-selective oxidation in CO_2 and/or H_2O is well documented, and the corresponding reaction mechanism has been widely studied, little is known about the early-stage of Fe-rich oxide nodule formation in these environments. Mechanistic descriptions have been published for reaction in air at elevated temperatures (1000–1200 °C) [19,20], but the specific influence of CO_2 and H_2O is yet to be determined.

This paper is aimed at investigating the evolution of oxide morphology and composition during the transition from Cr_2O_3 to Fe-rich oxide formation during oxidation of Fe–Cr and Fe–Cr–Ni alloys in dry and wet CO_2 atmospheres at 650 °C.

2 Experimental

Binary and ternary alloys of composition given in Table 1 were prepared by argon arc melting Fe (99.99 % pure), Cr (99.995 % pure) and Ni (99.95 % pure). Ingots were annealed in Ar–5%H_2 at 1150 °C for 48 h, and cut into rectangular samples of approximate dimensions 14 × 6 × 1.5 mm. The phase constitution of annealed materials determined by XRD analysis is indicated in Table 1. The single phase alloys had coarse-grained (∼ 500 μm) microstructures, while the two-phase alloys presented a finer (∼ 10 μm) γ–α substructure. Specimens were mechanically ground to a 1200 grit finish, degreased and ultrasonically cleaned in ethanol before reaction.

Isothermal corrosion experiments were conducted at 650 °C in Ar–20%CO_2, Ar–20%CO_2–5%H_2O and Ar–20%CO_2–20%H_2O mixtures at a total pressure of about 1 atm. Linear gas flow rates were set at about 2 cm s^{-1}. The wet gases were gener-

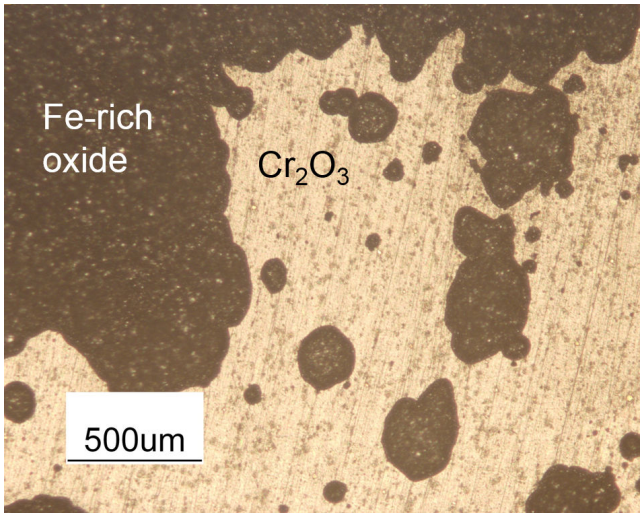

Figure 1: Surface view of Fe–20Cr after 120 h reaction in Ar–20CO_2.

ated by passing a mixture of Ar and CO_2 through a thermostatted water saturator. The distilled water in contact with the gas mixture was set at a temperature about 20 °C higher than that required to produce the nominal p_{H_2O}. Excess water vapour was subsequently condensed by cooling the wet gas in a distillation column. Oxygen partial pressures in these mixtures are so low ($\sim 1 \times 10^{-8}$ atm) that chromium volatilisation is negligible.

Reaction products were analysed by X-ray diffraction (XRD) using a Phillips X'pert Pro MPD diffractometer. Imaging and chemical analysis were carried out by optical microscopy (OM) and scanning electron microscopy combined with energy-dispersive X-ray spectroscopy (SEM-EDS), using a LEO 435VP microscope with PGT IMIX EDS system. Raman spectroscopy was performed using a Horiba Jobin–Yvon Labram HR 800 Raman microscope with an argon laser (wavelength 532 nm, power 20 mW), with a spatial resolution of 1 µm. The spectra of oxide phases in the Fe–Cr–O system were interpreted using the work of McCarty and Boehme [21], who studied Raman signatures of the spinel- ($Fe_{3-x}Cr_xO_4$) and corundum-type ($Fe_{2-x}Cr_xO_3$) solid solutions. The spectral resolution was 0.4 cm^{-1}, which allowed the oxide composition to be determined in a semi-quantitative way [21]. Metallographic observations were carried out on polished and etched cross-sections. Etching with Murakami's reagent (1 g $K_3Fe(CN)_6$ and 1 g KOH in 10 ml H_2O) revealed carbides.

3 Results

3.1 Overview

Exposure of Fe–20Cr, Fe–20Cr–10Ni, Fe–20Cr–20Ni and Fe–25Cr to dry and wet CO_2 resulted in non-uniform oxidation morphologies, as the alloys produced both a thin oxide scale and thicker oxide nodules characteristic of breakaway (Fig. 1). In contrast, Fe–25Cr–10Ni and Fe–25Cr–20Ni suffered no breakaway oxidation within the duration of the experiments, forming mainly a thin protective scale.

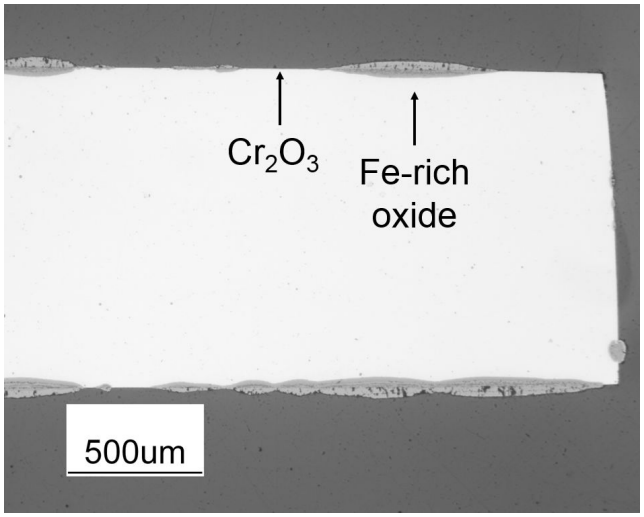

Figure 2: Optical microscope overview of oxidation products grown on Fe–20Cr after 80 h reaction in Ar–20CO_2.

Total weight gains and surface fractions of nodular oxide varied considerably; the effects of alloy and gas composition on the kinetics of breakaway oxidation are reported in a companion paper [22].

3.2 Reaction products

After reaction in both dry and wet CO_2, analysis by XRD of oxidised specimen surfaces revealed the presence of Cr_2O_3 as the only oxide in the case of Fe–25Cr–10Ni and Fe–25Cr–20Ni. Optical microscope examination of the specimen surfaces revealed the presence of isolated nodules, 1–30 µm large. The nodules covered a very small fraction of the surface area, and only the thin chromia scale was seen in metallographic cross-sections. After reaction of all other alloys in dry and wet CO_2, Cr_2O_3, Fe_2O_3 and Fe_3O_4 were detected by XRD. Individual nodules approximately circular in plan (Fig. 1) and elliptical in cross-section (Fig. 2), and extensive areas of iron oxide formation were observed, along with regions of protective chromia scale.

Fe–20Cr

During exposure to dry CO_2, the Fe–20Cr alloy produced a thin protective oxide scale and multilayer nodules, either isolated or forming semi-continuous scales of uniform thickness (Fig. 2). The only difference observed after exposure to Ar–20CO_2–5H_2O and Ar–20CO_2–20H_2O was that the extent of nodule formation was greater than in the dry gas, such that a multilayer scale of uniform thickness was observed on most of the cross-sections. Nodules appeared to be randomly distributed; in particular, nodule formation was not more important on the specimen edges than on the faces (see Fig. 2). On a given specimen, that is, after a given reaction time, nodules of various dimensions were observed. However, large nodules and uniform scales all had the same phase constitution, regardless of reaction time or gas composition.

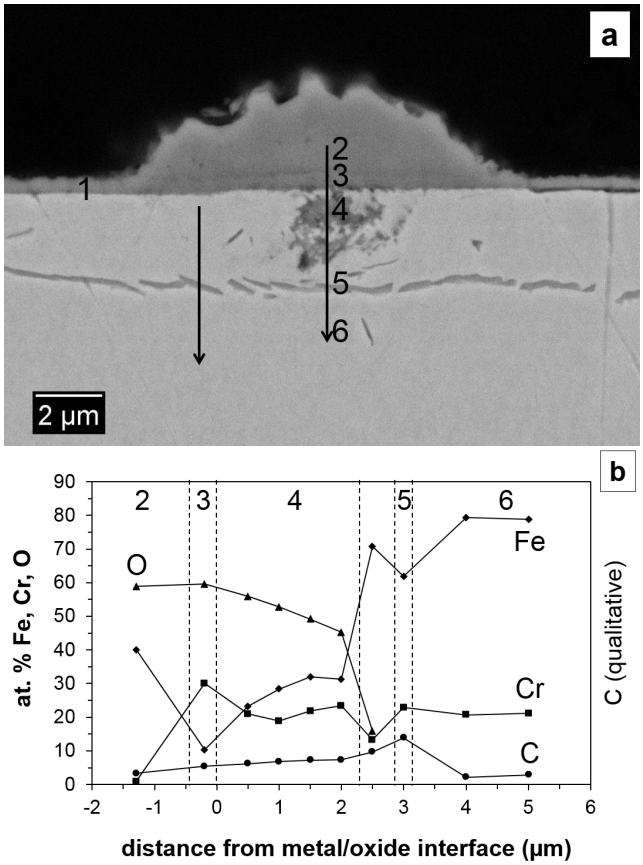

Figure 3: SEM-EDS analysis of newly formed Fe-rich oxide nodule on Fe–20Cr reacted 80 h in Ar–20CO_2. Specimen etched with Murakami's reagent. The right hand arrow and numbers in the BSE view (a) indicate the location of the profile in (b). The left hand arrow in (a) indicates the location of the profile marked by open square symbols (□) in Fig. 9e.

A small oxide nodule formed on Fe–20Cr after 80 h reaction in Ar–20CO_2 is shown in Fig. 3, along with an EDS profile recorded along the right hand arrow. The outer part of the nodule consists of iron oxide (zone 2), located above the originally protective scale; a chromium-rich oxide (zone 3) lies in a layer continuous with the protective scale surrounding the nodule; an internal oxidation zone with roughly equal concentrations of iron and chromium (zone 4) is found beneath the metal/oxide interface; and a semi-connected array of chromium-rich carbides lies in the narrow zone 5 parallel to the metal surface, under the internal oxides. Unreacted alloy (zone 6) lies beneath. The SEM-EDS results must be considered with caution: the analysis is quantitative only in the metal phase, and qualitative in oxide and carbide phases. Since the region probed is about 1 µm wide, when a point analysis is made on a smaller feature, part of the signal comes from the surrounding phase. In particular, for small Cr-rich features surrounded by Fe-rich environments, such as the internal oxide and carbide in zones 3 and 5, the Cr/Fe ratio is underestimated.

Raman spectra recorded on Fe–20Cr after 120 h reaction in Ar–20CO_2 from a similar nodule are shown in Fig. 4. Using data in Ref. [21], the protective scale (zone 1) is identified as Cr-rich M_2O_3, the nodule outer layer (zone 2) as Fe-rich

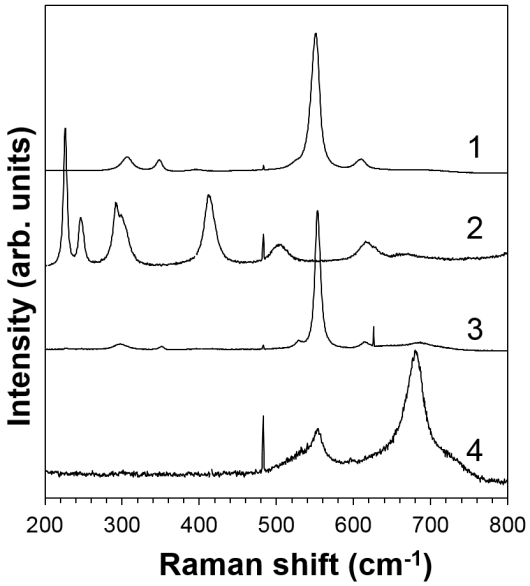

Figure 4: Raman spectra of oxide phases grown on Fe–20Cr reacted 120 h in Ar–20CO_2 (numbers correspond to zones defined in Fig. 3).

M_2O_3, the layer which is continuous with the protective scale (zone 3) as Cr-rich M_2O_3, and the internal oxide particles (zone 4) as Fe–Cr spinel. These phases are all consistent with the compositions determined with SEM-EDS. Data in Ref. [21] were used to construct the graph of Fig. 5, where the Raman shift of the A_{1g} symmetry (main band at 680–670 cm^{-1}) in the Fe–Cr spinel is plotted against the chromium content, expressed as x in $Fe_{3-x}Cr_xO_4$. A given Raman shift possibly corresponds to several compositions. The internal oxides (zone 4) present a Raman band at 680 cm^{-1}, which could correspond to $x = 0.3$, 0.9 or 1.6. On the basis of several EDS point measurements in the internal oxidation zone, the average Cr/Fe ratio yields $x = 1.3$, which must be underestimated, as discussed previously. The internal oxides are therefore identified as $Fe_{1.4}Cr_{1.6}O_4$.

A typical uniform multilayer scale observed on Fe–20Cr after 80 h reaction in dry CO_2 yielded the SEM images and the EDS profile shown in Fig. 6. Both outer layers (zones 7 and 8) consist of iron oxide. At the location of the original metal surface, a layer containing more chromium than the adjacent phases can still be distinguished (zone 9 in Fig. 6b). An intermediate layer of this sort is distinguished in all multilayer nodules and scales, and is always continuous with the protective Cr_2O_3 on the adjacent alloy surface. It is notable that this remnant of formerly protective Cr_2O_3 scale is never visibly disrupted by the iron-rich oxide, as shown in Fig. 7. The inner layer is a two-phase mixture (zone 10 in Fig. 6c) containing iron and chromium. Beneath it lies an internal oxidation area (zone 11). The volume fraction of internal oxides, f_{V-ox}, varied with location in a given specimen, but did not change significantly with gas composition or reaction time. Image analysis after reaction in dry and wet CO_2 yielded $f_{V-ox} = 0.7 \pm 0.1$.

The Raman spectra in Fig. 8 were recorded in zones corresponding to those described above, after 120 h reaction of Fe–20Cr in dry CO_2. Using data in Ref. [21], the outermost layer was identified as Fe_2O_3, and all other oxides as spinel phases.

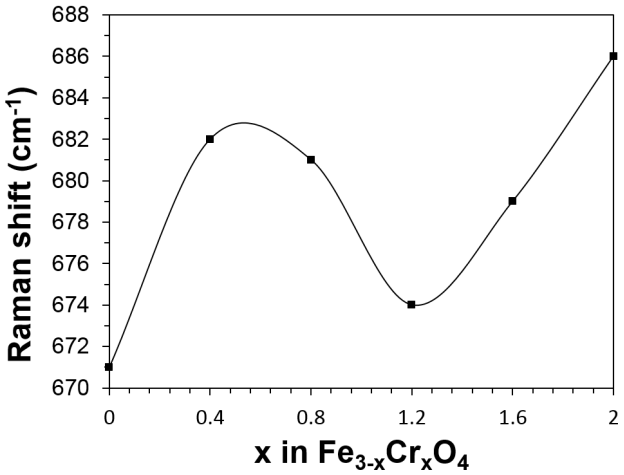

Figure 5: Main Raman shift of Fe–Cr spinel oxide as a function of composition, data from Ref. [21].

The outer spinel layer (# 8) features a main band at 671 cm^{-1}, characteristic of pure Fe_3O_4. The thin intermediate layer (# 9) has a main band at 680 cm^{-1}, which could correspond to $x = 0.3$, 0.9 or 1.6. Since EDS provides $x = 1.6$, the phase is identified as $Fe_{1.4}Cr_{1.6}O_4$. The inner two-phase mixture (# 10) had a main Raman band at 674 cm^{-1}, corresponding to $Fe_{2.9}Cr_{0.1}O_4$ or $Fe_{1.8}Cr_{1.2}O_4$. These two compositions may well reflect the two spinel phases present in the inner layer. Indeed, the isothermal section of the Fe–Cr–O phase diagram at 627 °C calculated in Ref. [23] predicts that the two coexisting spinels are $Fe_{2.7}Cr_{0.3}O_4$ and $Fe_{1.8}Cr_{1.2}O_4$. Chemical analysis in the inner layer yielded $x = 1.3$, implying that the iron-rich spinel is present in very small quantity. In the internal oxidation zone (# 11), three compositions are possible from the Raman spectrum, with $x = 0.3$, 0.8 or 1.7. At the low p_{O_2} of the internal oxidation zone, the highest chromium spinel $Fe_{1.3}Cr_{1.7}O_4$ is the only valid candidate (see phase diagram in Ref. [23]).

The Fe–20Cr alloy also suffered carburisation. Internal precipitates were revealed by etching with Murakami's reagent, and identified as carbides by SEM-EDS. Raman signals were obtained from the carbides. However, as no reference data were found, these spectra could not be interpreted. The precipitate morphology and penetration depth varied with the nature of the overlaying oxide. Intergranular carbides were found throughout reacted specimens, from the shortest exposure time (40 h). Underneath Cr_2O_3 scales, intragranular carburisation was either absent or limited to a more or less continuous plate (zone 5 in Fig. 3), parallel to the alloy surface at a shallow (< 20 µm) depth. The thickness of this plate was approximately constant with time between 40 and 120 h. The formation of nodules was independent of the presence or absence of intragranular carbides underneath the surrounding Cr_2O_3. Intragranular carbides were present beneath most, but not all, of the small nodules. Once the Fe-rich oxide became more or less uniform in thickness, intragranular carburisation was extensive (zone 12 in Fig. 6), with penetration depths of about 100 µm in 240 h of reaction. Carburisation results have been reported in more detail elsewhere [24].

Chromium depletion profiles underneath the protective Cr_2O_3 scale grown on

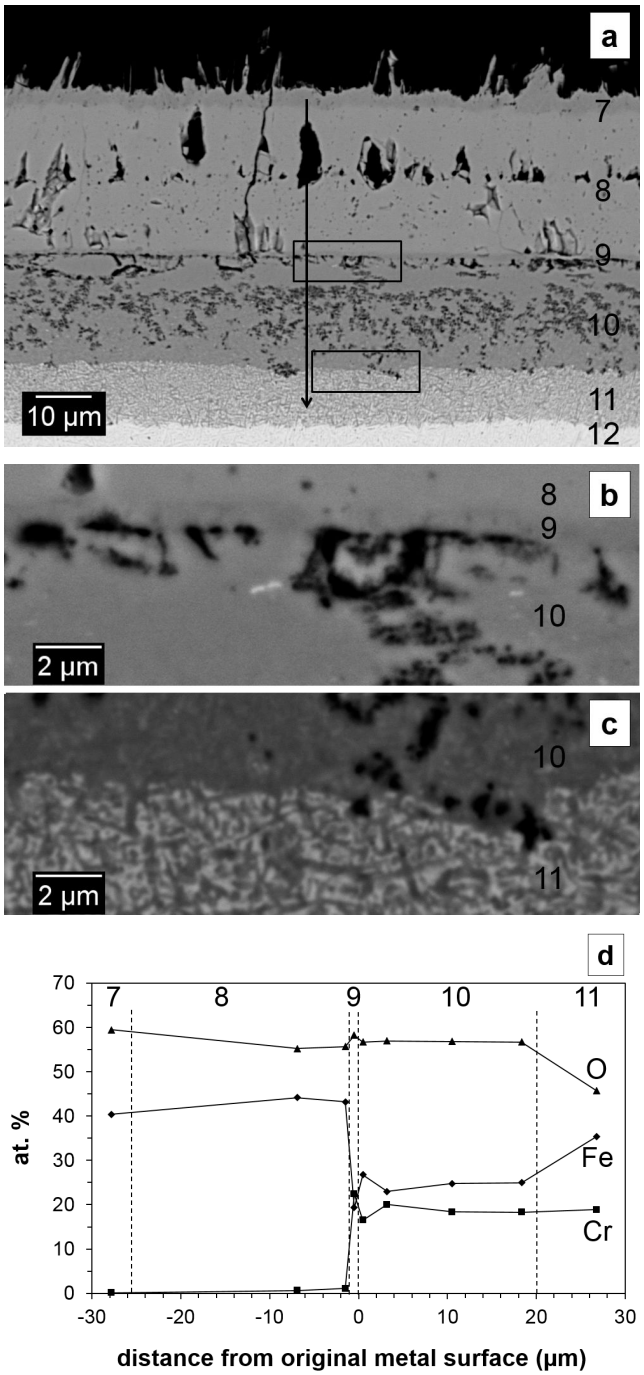

Figure 6: SEM-EDS analysis of Fe-rich oxide scale grown on Fe–20Cr reacted 80 h in Ar–20CO_2. Specimen etched with Murakami's reagent. The boxes and arrow in the BSE view (a) indicate the location of the images and profile in (b), (c) and (d).

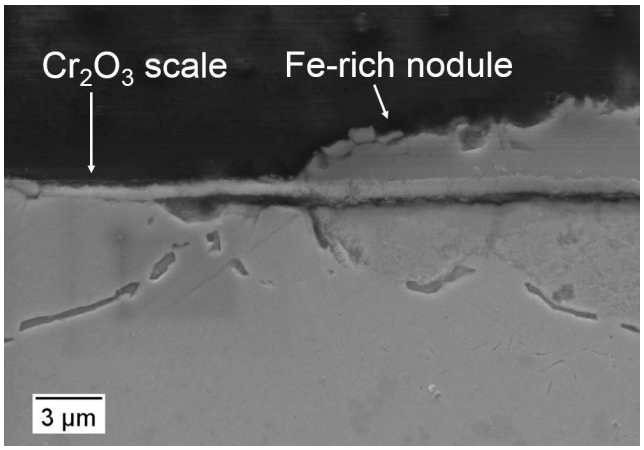

Figure 7: SEM image (SE mode) showing the continuity of protective Cr_2O_3 scale with the intermediate layer of the nodule in Fe–20Cr after 80 h reaction in Ar–20CO_2. Specimen etched with Murakami's reagent.

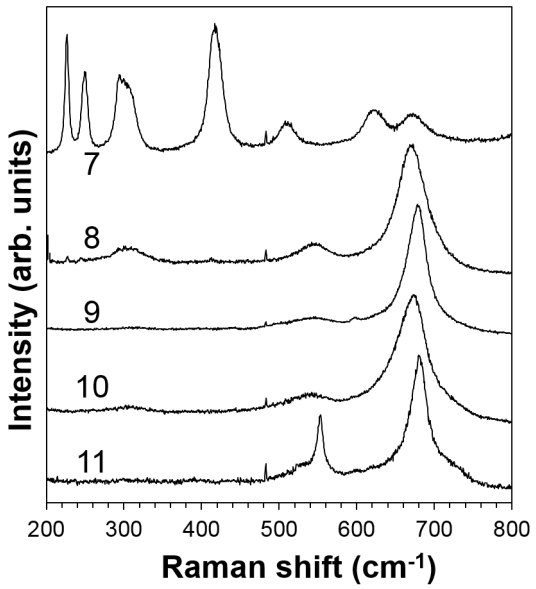

Figure 8: Raman spectra of oxide phases in Fe-rich multilayer oxide grown on Fe–20Cr reacted 120 h in Ar–20CO_2 (numbers defined in Fig. 6).

the Fe–20Cr alloy after 80 h exposure to dry CO_2 were measured using SEM-EDS, in several carbide-free (e.g. Fig. 9a) and carbide-containing (e.g. Fig. 9b) zones. The profiles thus recorded are grouped according to the local Cr_2O_3 scale thickness in Fig. 9c–e, with results from carbide-free and carbide-containing regions represented by filled and open symbols, respectively. The reproducibility of the measured chromium concentration profiles was very good for a given scale thickness, as shown in Fig. 9c–e. The same measurements were made after exposure of the Fe–20Cr alloy to Ar–20CO_2–20H_2O (not shown here). No difference in chromium depletion could be seen between reaction in dry and wet gas, and similar Cr_2O_3 scale thicknesses were observed in both cases.

Fe–25Cr

The Fe–25Cr alloy formed different oxidation products (Fig. 10), which can be classified in three morphological types (Fig. 11): a thin protective scale, thick multilayer nodules and multilayer oxides of intermediate thickness, referred to as "healed scale". Thicker nodules were observed to form preferentially on the specimen edges. The only difference between products formed in different reaction gases was the proportion of each oxide type.

Raman spectra obtained from a specimen reacted 240 h in Ar–20CO_2 are shown in Fig. 12 for the locations indicated in Fig. 11. The protective scale (zone 1) is Cr-rich M_2O_3. On the healed scales (Fig. 11a), the outer layers are Fe-rich M_2O_3 (zone 2) and M_3O_4 (zone 3). The inner layer (zone 4) is a spinel, with a main band at 678 cm^{-1}, corresponding to $x = 0.2$, 1 or 1.5 in $Fe_{3-x}Cr_xO_4$. Chemical analysis using SEM-EDS was performed on this layer at several equivalent locations (not shown). The results varied considerably with analysis location, with Cr/Fe ratios ranging from 1.76 to 12.3. While the lower value would correspond to $Fe_{1.1}Cr_{1.9}O_4$, the higher values indicate a Cr-rich corundum type oxide, $Fe_{2-x}Cr_xO_3$, with an average $x = 1.8$. Considering Raman and EDS results, it is concluded that the inner layer may be of spinel or corundum type, with varying composition, but always relatively rich in chromium. Internal oxidation was never observed underneath this type of scale.

On the thick nodules (Fig. 11b), the outer layers are also Fe_2O_3 (zone 5) and Fe_3O_4 (zone 6). The thin intermediate layer (zone 7) is a spinel with a main Raman band at 680 cm^{-1}, corresponding to $x = 0.3$, 0.9 or 1.6. In view of the results presented above for Fe–20Cr, the Cr-richer composition is the most likely. Finally, the inner layer (zone 8) is a spinel with a main band at 674 cm^{-1}, which again is interpreted as a $Fe_{2.9}Cr_{0.1}O_4$ + $Fe_{1.8}Cr_{1.2}O_4$ mixture. An oxide + metal mixture is apparent (zone 9) below the inner layer, but it was not possible using metallographic observation to ascertain whether the oxide was detached from the inner layer (i.e. internal oxidation) or in continuous contact (i.e. protrusions of the inner layer into the metal). In either case, the volume fraction of oxide was very high.

After exposure to dry CO_2, intragranular carbides were found at scattered locations underneath the protective Cr_2O_3 scale and the healed scale, with a penetration depth less than 5 μm. Beneath the thick nodules, the alloy produced intragranular carburisation zones (zone 10 in Fig. 11b), about 50–70 μm deep after 240 h, and intergranular carbides were found to great depths (see Fig. 10). After exposure to Ar–20CO_2–20H_2O, however, carbides were absent below Cr_2O_3 and the healed scale.

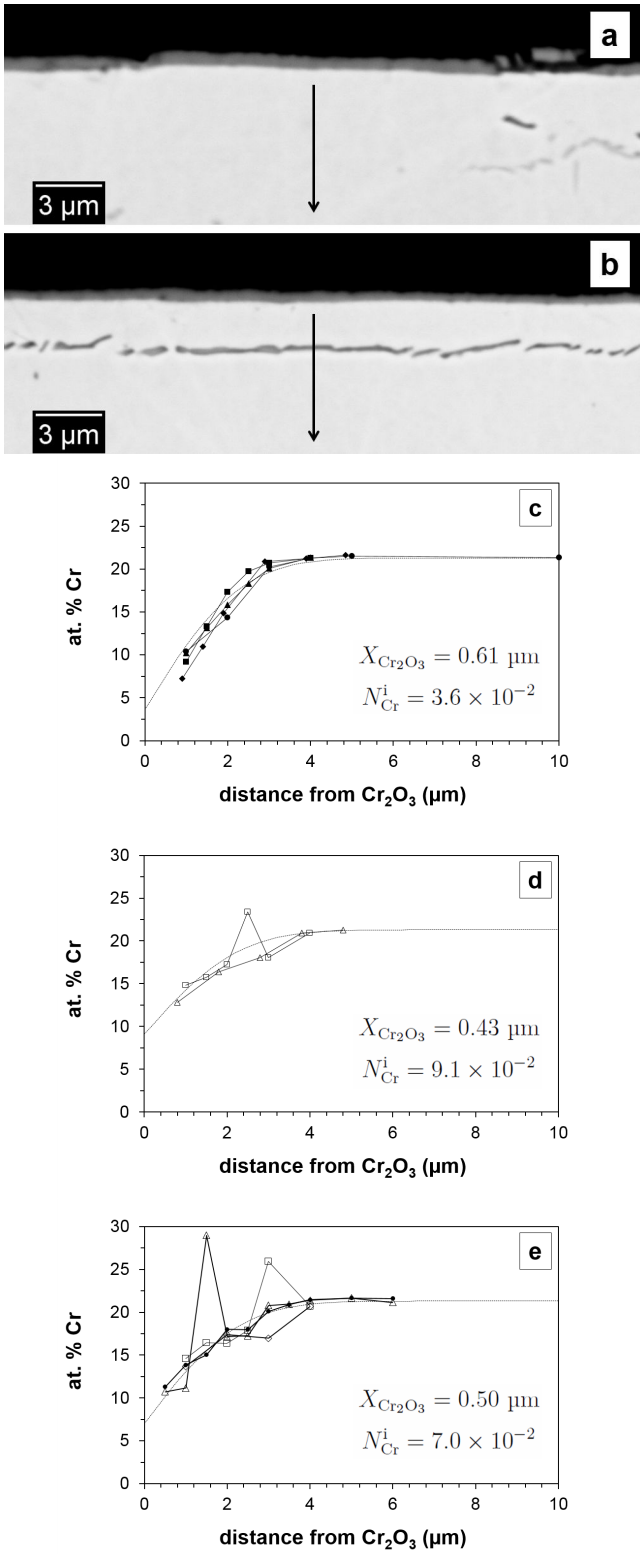

Figure 9: SEM-EDS analysis of Cr-depleted zone underneath Cr_2O_3 grown on Fe–20Cr reacted 80 h in Ar-20CO_2. Specimen etched with Murakami's reagent. (a–b) BSE images; (c–e) Cr concentration profiles. Experimental profiles (point symbols) were recorded in different locations. Filled symbols: carbide-free locations, e.g. SEM view (a); open symbols: scans which traverse carbides as in SEM view (b). Symbols (□) in (e): profile marked by the LHS arrow in Fig. 3a. Dashed lines were calculated from Eq. (6).

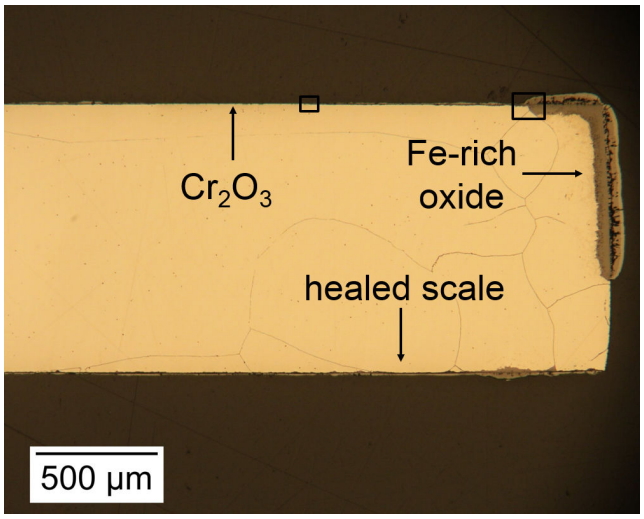

Figure 10: Optical microscope overview of oxidation products grown on Fe–25Cr after 240 h reaction in Ar–20CO_2. Specimen etched with Murakami's reagent. The two black boxes indicate the locations of the images in Fig. 11.

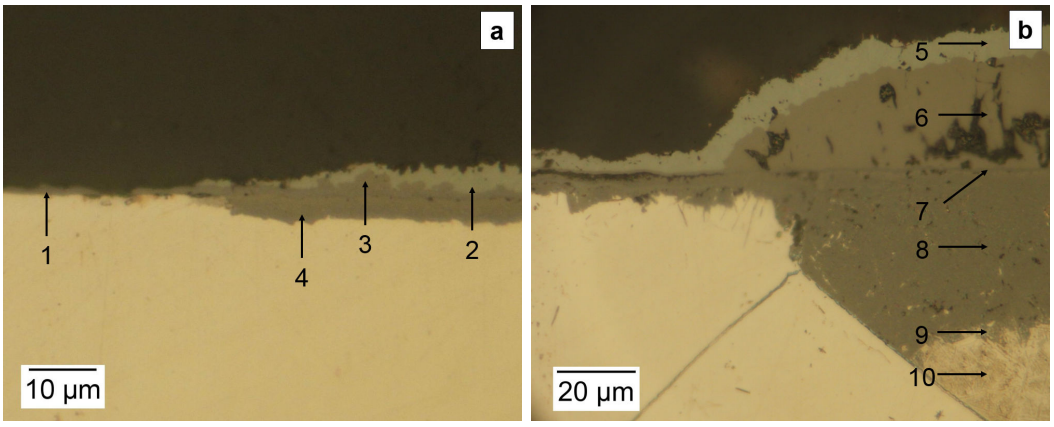

Figure 11: Optical microscope views of oxides grown on Fe–25Cr after 240 h reaction in Ar–20CO_2. Specimen etched with Murakami's reagent. (a) protective Cr_2O_3 and healed scale; (b) healed scale and Fe-rich multilayer oxide.

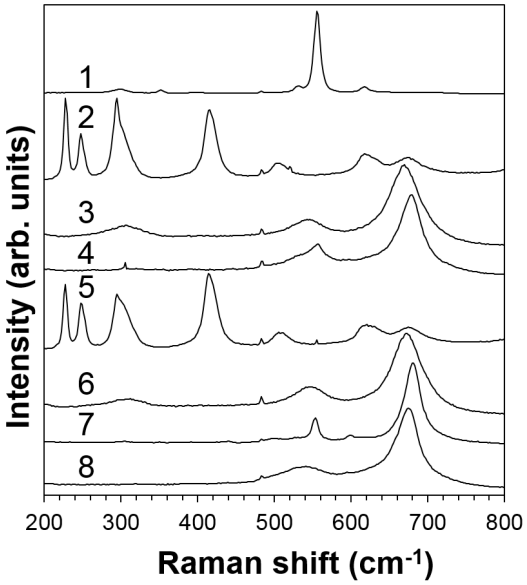

Figure 12: Raman spectra of oxide phases on Fe–25Cr after 240 h reaction in Ar–20CO_2. The numbers refer to Fig. 11.

Underneath the thick nodules, intergranular carbides were sparsely distributed, and the intragranular carbide volume fractions and penetration depths (about 30–50 µm after 240 h) were lower than observed after exposure to the dry gas.

Fe–20Cr–10Ni and Fe–20Cr–20Ni

The Fe–20Cr–10Ni and Fe–20Cr–20Ni alloys formed a protective oxide scale and oxide nodules of varying dimensions. The nodules were on average thicker on the 10Ni alloy. Individual nodules developed the same morphology on both alloys in both dry and wet CO_2.

Raman analysis showed that the protective scales grown on the two alloys were Cr_2O_3 (not shown here). Nodule constitution was studied on an Fe–20Cr–10Ni specimen reacted in dry CO_2 using SEM imaging, EDS and Raman analysis (Fig. 13). The outer layers consist of Fe_2O_3 (zone 1) and Fe_3O_4 (zone 2), with no significant amount of dissolved chromium or nickel. It was not possible to ascertain whether a thin intermediate Cr-rich layer was still present at the original metal surface. It was either too thin to be clearly distinguished, or sometimes apparent but disrupted. The inner layer (zone 4) contains at least two phases, but might have contained three; this was difficult to determine using SEM, because of the extremely fine microstructure. The Raman spectrum (Fig. 13c) recorded in the inner layer shows a broad band which could be deconvoluted into two peaks at approximately 684 and 712 cm^{-1}. The former peak can be associated with either a Cr-rich Fe–Cr spinel [21] or $NiCr_2O_4$ [25], and the latter peak with $NiFe_2O_4$ [25]. This area is seen using EDS results (Fig. 13b) to contain 24 at. % iron, 19 at. % chromium and 7 at. % nickel. Assuming that spinels of the precise stoichiometries $FeCr_2O_4$, $NiCr_2O_4$ and $NiFe_2O_4$ are present, then solving a simple 3 variable, 3 equation system yields the proportions of the spinel phases: 56.3, 0.5 and 43.2 mol %, respectively. Given the

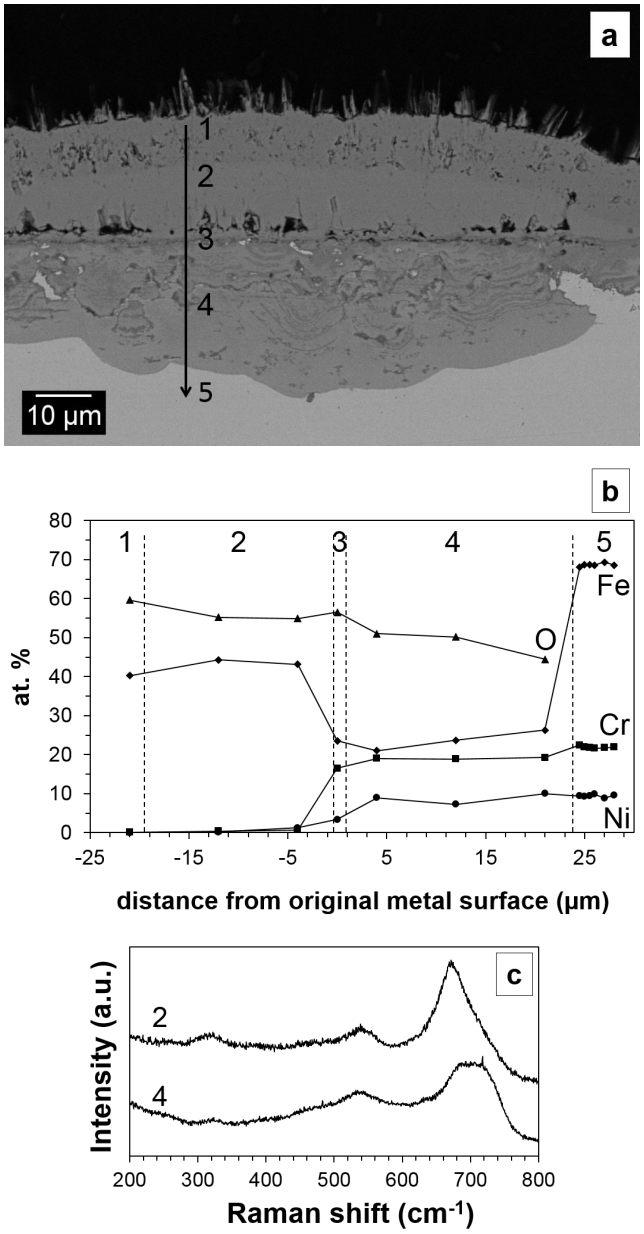

Figure 13: (a) SEM BSE image, (b) SEM-EDS and (c) Raman analysis of multilayer oxide grown on Fe–20Cr–10Ni after 240 h reaction in Ar–20CO_2. Specimen etched with Murakami's reagent. The numbers in (b) and (c) correspond to the zones marked in (a).

uncertainty in the Raman and EDS results, the inner layer may be approximated as a $NiFe_2O_4$–$FeCr_2O_4$ mixture.

The Fe–20Cr–10Ni and Fe–20Cr–20Ni alloys showed no internal oxidation. The Fe–20Cr–10Ni alloy occasionally developed intergranular carbides, but no intragranular carbides, after exposure to dry CO_2, and no carbides at all after exposure to wet CO_2. The Fe–20Cr–20Ni alloy underwent no carburisation in any of the gases.

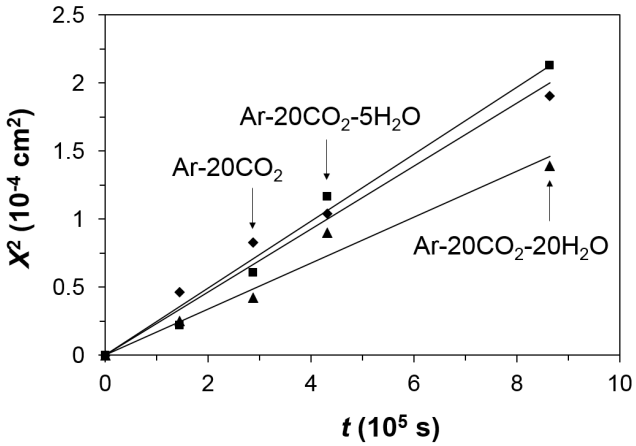

Figure 14: Iron-rich oxide thickening kinetics measured on Fe–20Cr.

Table 2: Fe-rich oxide thickening rate constant, $k_{p,\mathrm{Fe-ox}}$ (10^{-11} cm^2 s^{-1}).

	Ar–20CO$_2$	Ar–20CO$_2$–5H$_2$O	Ar–20CO$_2$–20H$_2$O
Fe–20Cr	12	12	8.5
Fe–20Cr–10Ni	3.1		
Fe–20Cr–20Ni			1.0
Fe–25Cr (thick nodules)	6.7		5.1
Fe–25Cr (healed scale)	0.069		0.069

3.3 Iron-rich oxide growth rate

Maximum nodule thickness measured after time-lapse exposures of Fe–20Cr to the dry and wet gases are reported in Fig. 14. Thickening kinetics are seen to follow approximately parabolic kinetics:

$$X^2 = 2k_{p,\mathrm{Fe-ox}}t \tag{1}$$

where X is the oxide thickness and $k_{p,\mathrm{Fe-ox}}$ the parabolic rate constant. The poor reproducibility of breakaway did not allow the influence of gas composition to be clearly determined on the basis of the $k_{p,\mathrm{Fe-ox}}$ values, which are given in Table 2. Rate constants as defined in Eq. (1) were estimated using a limited number of specimens of the three other alloys prone to breakaway oxidation; approximate values are given in Table 2. In the case of Fe–25Cr, the kinetics were measured for both healed scales and thick nodules.

In Fig. 15, the thickness of individual nodules is plotted against their diameter. Diameter and thickness are seen to be proportional, and the proportionality constant characterising the nodule morphology is independent of gas and alloy composition. Lateral growth kinetics may thus be approximated as:

$$r^2 = 2k_l\, t \tag{2}$$

where r is the nodule radius and k_l the lateral growth rate constant ($k_l = 0.73k_{p,\mathrm{Fe-ox}}$ for all alloys and gases).

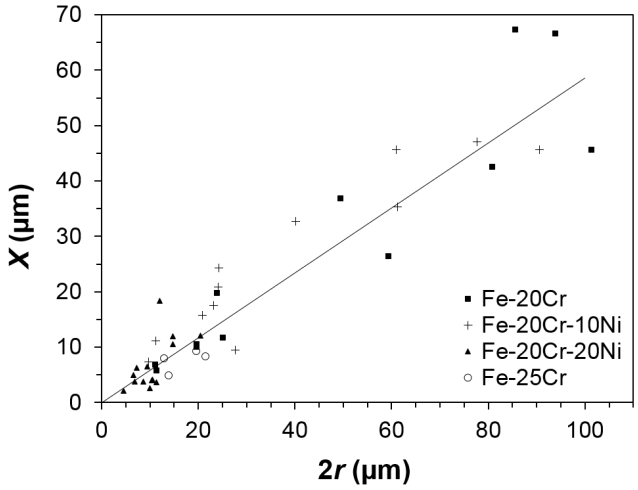

Figure 15: Morphology of nodules grown on various alloys, regardless of the gas composition.

4 Discussion

The evolution of oxide morphology during breakaway can be summarised as follows. Initially, a protective Cr_2O_3 scale is formed on the alloy surface. At certain locations, Fe_2O_3 grows on top of the chromia, and simultaneously the alloy is oxidised beneath it. Individual nodules thicken and spread laterally, and then coalesce to form continuously thick Fe-rich oxide scales.

The conditions underlying Cr_2O_3 failure and nodule development are examined in the following subsections.

4.1 Chromium depletion and influence of carburisation on breakaway

The chromium concentrations measured in subsurface zones of Fe–20Cr in regions of protective oxidation (Fig. 9) are sensitive to the thickness of the Cr_2O_3 scale located directly above, and this varied with location. In order to rationalise the results, chromium concentrations were calculated using the classical one-dimensional diffusion analysis of the depletion problem.

Chromium depletion was limited to about 5 µm, whereas the specimens were more than 1 mm thick. Clearly, at the low experimental temperature, Cr_2O_3 growth is too slow for the depletion profiles generated on the opposed faces of a specimen to overlap in the time frame considered. Interfacial chromium mole fractions were calculated on the assumption that the scale is pure Cr_2O_3, using the steady-state equation given by Wagner [26]:

$$\frac{N^0_{Cr} - N^i_{Cr}}{1 - N^i_{Cr}} = F\left(\frac{2V_{alloy}}{V_{Cr_2O_3}}\sqrt{\frac{k_{p,Cr_2O_3}}{D_{Cr}}}\right) \tag{3}$$

where N^0_{Cr} is the initial chromium mole fraction, V the molar volume ($V_{alloy} = 7.1$ cm^3 mol^{-1} and $V_{Cr_2O_3} = 29$ cm^3 mol^{-1}), D_{Cr} the chromium diffusion coefficient ($D_{Cr} = 5.61 \times 10^{-14}$ cm^2 s^{-1} at 650 °C, extrapolated from data in Ref. [27]), and F

a function defined by:

$$F(u) = \sqrt{\pi}u(1 - \operatorname{erf} u)\exp\left(u^2\right) \tag{4}$$

Oxide growth is described by the rate law:

$$X^2_{Cr_2O_3} = 2k_{p,Cr_2O_3}t \tag{5}$$

using k_{p,Cr_2O_3} to denote the Cr_2O_3 rate constant. Molar volumes and diffusion coefficient are assumed not to vary with alloy composition. Since the experimental values were sensitive to the thickness of the oxide located directly above, values were estimated for each location using the measured oxide thickness and reaction time. Values of N^i_{Cr} deduced from Eq. (3) were then used to calculate depletion profiles using the appropriate solution of Fick's second law of diffusion for a semi-infinite solid [28]:

$$\frac{N_{Cr}(x,t) - N^i_{Cr}}{N^0_{Cr} - N^i_{Cr}} = \operatorname{erf}\left(\frac{x}{2\sqrt{D_{Cr}t}}\right) \tag{6}$$

where x is the distance from the metal/oxide interface. The calculated profiles are shown as dashed lines in Fig. 9c–e.

Chromium depletion profiles recorded in carbide-free zones (filled symbols in Fig. 9c–e) are seen to match very well the calculated profiles. Significant changes in N^i_{Cr} are seen to accompany local variations in scale thickness on the same specimen. The need to use local k_{p,Cr_2O_3} values in the calculation is clear. The success of Eq. (3) in relating chromium depletion to chromia scaling rate, despite local variations in the two quantities, demonstrates that the mass balance underlying the equation is correct. In other words, the composition of the protective scale does not change significantly, and variations in its growth rate have some other cause. As diffusion in chromia scales at this temperature is predominantly via grain boundaries [29], it seems likely that local variations in oxide grain size and/or shape are responsible for altered scaling rates. However, no information is available from the present work.

The observed variations in $X_{Cr_2O_3}$ and N^i_{Cr} along the scale interface are significant. Although the steady-state analysis of Eqs. (3–6) succeeds when applied locally, the alloy-scale system as a whole is characterised by a boundary condition which varies with lateral position. Thus the system is not in a uniform steady state. Rather, it should be thought of as subject to fluctuations which are not quickly removed. The process for their removal – lateral diffusion of alloy chromium parallel to the scale interface – is slow compared to chromium diffusion toward the scale, because the concentration gradients involved are smaller.

Carburisation affects the concentration profiles in that whenever it occurred, the chromium concentration is seen to be higher than the predicted value in the carbide, and slightly lower in the surrounding matrix. This merely reflects the fact that the carbides are chromium-rich. However, away from the carbides, the depletion profiles are entirely determined by the thickness of the overlaying Cr_2O_3 scale. Depletion profiles recorded after exposure to Ar–20CO_2–20H_2O (not shown here) were closely similar: N^i_{Cr} values were similar, and related in the same way to $X_{Cr_2O_3}$, independently of whether or not carbide precipitated.

The results demonstrate that in the conditions of interest, the limited carbide precipitation which occurs in Fe–20Cr below a protective Cr_2O_3 scale does not affect

chromium depletion. In particular, the interfacial concentration, which is critical to the resistance of the alloy to breakaway, remains unchanged. Evidently the Cr_2O_3 scale is a rather good (but not perfect) barrier to carbon entry into the alloy. The plate-like morphology of the carbides indicates that when it formed early in the reaction, the inward carbon flux was small, allowing the relatively large chromium flux to favour precipitate growth and coalescence over new nucleation. Subsequently, the carbide plate was observed not to thicken (over 40–120 h), indicating that no further carbon uptake was occurring in the alloy. In the absence of precipitation beneath the carbide plate, the chromium concentration in the matrix, and therefore the driving force for outward chromium diffusion, are globally unaffected by carburisation.

Precipitation occurs where the carbide solubility product is exceeded. This condition defines a distance x_{carb} from the alloy/Cr_2O_3 interface, below and above which no carbide is found: for $x < x_{carb}$, N_{Cr} is too low because of oxidation-induced depletion, and for $x > x_{carb}$, N_C is too low because carbon is almost entirely precipitated. The critical chromium mole fraction for carburisation, $N_{Cr,carb}$ is determined by the interfacial carbon activity and carbide composition. In the absence of carbon activity data, $N_{Cr,carb}$ may be estimated as 0.2 from the experimental profiles of Fig. 9. Using a phase diagram of the Fe–Cr–C system generated with Thermo-Calc [30] and the TCFE4 database, one finds the carbides forming in the depletion zone to be Cr-rich $M_{23}C_6$, with $a_C = 8 \times 10^{-4}$ at the alloy/carbide interface. This is much lower than the value expected from thermodynamic equilibrium at the metal/oxide interface [24], confirming that the scale provides a partial barrier to carbon entry.

Combining Eqs. (3), (5) and (6), $N_{Cr,carb}$ is written:

$$N_{Cr,carb}(x,t) = \frac{N^0_{Cr} - f\left(X_{Cr_2O_3}\right)}{1 - f\left(X_{Cr_2O_3}\right)}\left[1 - g\left(x_{carb}\right)\right] + N^0_{Cr} g\left(x_{carb}\right) \tag{7}$$

where

$$g(x) = \operatorname{erf}\left(\frac{x}{2\sqrt{D_{Cr}t}}\right) \tag{8}$$

$$f\left(X_{Cr_2O_3}\right) = F\left(\frac{V_{alloy}}{V_{Cr_2O_3}}\frac{X_{Cr_2O_3}}{\sqrt{D_{Cr}t}}\right) \tag{9}$$

and F is the function defined in Eq. (4). Equation (7) was solved numerically to obtain x_{carb} as a function of $X_{Cr_2O_3}$ and t. The result is shown in Fig. 16, together with experimental values measured on Fe–20Cr after reaction in Ar–20CO_2. The essential prediction of Eq. (7) is that as Cr_2O_3 grows and chromium depletion extends into the alloy, the carbide plate moves inward, and this is indeed observed experimentally for short reaction times. It is proposed that at steady-state, formation-dissolution of the carbide plate is responsible for its inward displacement and enables the global outward chromium flux to remain unaltered, thus accounting for the fact that N^i_{Cr} is the same in the presence or absence of carburisation. However, this model fails to describe the data after 120 h reaction, where the carbide plate is formed deeper within the alloy, beneath the chromium depletion zone.

The universal occurrence of extensive carburisation beneath large nodules and regions of uniformly thick Fe-rich oxide shows that this material is significantly more permeable to carbon than is Cr_2O_3, as noted by previous investigators [2]. The fact that extensive carburisation was never found in the absence of Fe-rich oxide, together with the observation that a number of early-stage nodules had no carbide beneath

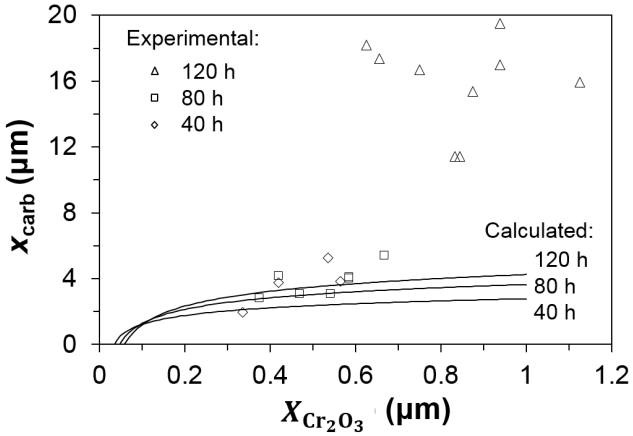

Figure 16: Distance of carbide plate from alloy/Cr_2O_3 interface in Fe–20Cr after exposure to Ar–20CO_2. Solid lines obtained from numerical solution of Eq. (7).

them, indicates that fast carbon ingress into the alloy is a consequence of breakaway oxidation, rather than a precursor.

Freshly formed nodules were observed in regions where carburisation did not occur beneath the surrounding Cr_2O_3 scale. Similarly, in the case of Fe–25Cr, Fe–20Cr–10Ni and Fe–20Cr–20Ni, carburisation was almost completely absent below the protective Cr_2O_3 scale, but the alloys formed Fe-rich oxide nodules (see for example Fig. 11a). Thus chromium-rich carbide precipitation is not a necessary condition for breakaway.

Giggins and Pettit [2] found that at 900 °C, a model Fe–15Cr alloy formed a protective oxide scale in O_2, but produced a rapidly growing Fe-rich oxide scale and internal carbides in CO_2. Furthermore, precarburisation and subsequent exposure to O_2 also resulted in breakaway, with the same rate and morphology as in CO_2. The authors concluded that carbide precipitation lessened the outward chromium flux and prevented external Cr_2O_3 growth. However, their precarburisation experiment produced a situation of massive internal carbide precipitation and a heavily depleted alloy matrix.

In contrast, Fe–20Cr reaction in CO_2 at 650 °C is found here initially to lead to Cr_2O_3 formation and only limited carburisation, leaving an outward chromium flux sufficient to sustain the scale growth. This protective behaviour is thus expected to be maintained under steady-state conditions, that is, as long as the scale permeability to oxygen and carbon is unaltered, and as long as it remains mechanically intact. Nonetheless, the alloy ultimately went into breakaway. An Fe–20Cr specimen from the same alloy batch used for CO_2 reaction was reacted in dry air at 650 °C for 336 h, and did not suffer breakaway. Clearly then, breakaway in CO_2 must be accelerated by carbon, although carbide precipitation beneath Cr_2O_3 is not of itself a sufficient condition. Further discussion requires the conditions for Cr_2O_3 failure to be defined.

4.2 Mode of Cr_2O_3 failure

Breakaway follows from the alloy's inability to maintain growth of the protective scale. The case of Cr_2O_3-forming alloys has been extensively discussed, for example in Refs. [18–20]. Chemical failure occurs when the chromium activity at the alloy/Cr_2O_3 interface is low enough for the reaction:

$$\underline{\mathrm{Fe}} + \frac{4}{3}\mathrm{Cr_2O_3} = \frac{2}{3}\underline{\mathrm{Cr}} + \mathrm{FeCr_2O_4} \tag{10}$$

to proceed. Since the chromium concentration involved is small, the solvent iron is approximated as pure ($a_{\mathrm{Fe}} = N_{\mathrm{Fe}} = 1$), and the law of mass action for reaction (10) is written:

$$K_{10} = \exp\left(\frac{-\Delta_f G^0_{\mathrm{FeCr_2O_4}} + \frac{4}{3}\Delta_f G^0_{\mathrm{Cr_2O_3}} - \frac{2}{3}\Delta\bar{G}^{xs}_{\mathrm{Cr}}}{RT}\right) \tag{11}$$

where $\Delta_f G^0_i$ is the standard free energy of formation of oxide i, and $\Delta\bar{G}^{xs}_{\mathrm{Cr}}$ the excess free energy of mixing for chromium solution in the metal matrix. The critical chromium atom fraction for Cr_2O_3 stability, N^*_{Cr}, is thus calculated from standard free energies [31] and dissolution data [32] to be 1.2×10^{-5} at $T = 650$ °C.

To sustain selective chromia formation, it is necessary that Cr_2O_3 be both thermodynamically and kinetically stable. Wagner [26] showed that the condition for an alloy chromium flux sufficient to maintain exclusive chromia growth is met if application of Eq. (3) yields values of $N^i_{\mathrm{Cr}} \geq 0$. Thermodynamic stability further requires that $N^i_{\mathrm{Cr}} \geq N^*_{\mathrm{Cr}}$; these requirements are essentially the same given the value of N^*_{Cr}. In all cases where a protective chromia scale is retained, then by definition the condition is met. Evaluation of is nonetheless useful, as it provides a guide as to how close an alloy might be to breakaway. In the case of Fe–20Cr reacted in dry CO_2, Eq. (3) yields $N^i_{\mathrm{Cr}} = (6.9 \pm 4.6) \times 10^{-2}$, where the average and standard deviation were calculated from a large number (84) of experimental values, measured after 40–240 h of reaction. The surplus of chromium is variable and sometimes small. Similar values were obtained from specimens reacted in wet CO_2. In the case of Fe–25Cr exposed to both dry and wet CO_2, values of calculated from local and Eq. (3) were about 10–15 at. %, in reasonable agreement with EDS measurements (not shown here), and far above the critical value, N^*_{Cr}. In the case of the ternary alloys, meaningful values of D_{Cr} are not available, because short-circuit (grain boundary and dislocation) diffusion prevails at the low reaction temperature of 650 °C [33]. Indeed, the 10Ni alloys possess a fine $\alpha + \gamma$ structure, and in the fully austenitic 20Ni alloys, the effects of cold working in the subscale region are likely to be still present at 650 °C [34]. In the absence of D_{Cr} values, no estimate of N^i_{Cr} is possible.

Under steady-state conditions then, the Fe–20Cr alloy is in some locations heavily depleted, but the Fe–25Cr alloy only moderately so. Nonetheless, both alloys suffered short-term breakaway. It is recognised that the diffusional steady-state described by Eqs. (3–6), and experimentally observed in Fe–20Cr and Fe–25Cr (e.g. Fig. 9) is predicted to endure until depletion reaches the specimen center. As alloy depletion zones were very shallow (e.g. Fig. 9), such an outcome was remote under the conditions considered here. Thus steady-state chromia scale growth, once established, is predicted to remain in effect within the experimental time frame. Clearly, this prediction failed for the alloys examined here.

Scale cracking or spallation can expose the depleted alloy to the reacting gas. Reformation of chromia at the relatively fast rate typical of initial growth causes an increase in the outward chromium flux, and N^i_{Cr} first decreases before returning to the steady-state value [35]. If N^i_{Cr} falls below N^*_{Cr} during the transient stage, chemical failure occurs.

No steady state description can encompass the onset of breakaway. However, examination of Eq. (3) reveals that the steady-state description loses applicability if k_{p,Cr_2O_3} changes, leading to a change in the boundary value and, by definition, a change in the reaction state. As discussed already, varies with position on the same specimen, and fluctuations in chromia growth rate must therefore be considered. Although the origins of these fluctuations are obscure, their consequences can be anticipated. Locally increased scaling rates can accelerate mechanical failure of the scale as growth stresses rise with increasing scale thickness. The lower value of induced by faster scaling means that scale cracking or spallation can allow gas access to a more heavily depleted alloy surface which cannot then repassivate. More simply, a sufficient increase in will render the scale kinetically unstable, because of limited alloy diffusion. In the case of Fe–20Cr, the N^i_{Cr} values calculated from Eq. (3), $(6.9 \pm 4.6) \times 10^{-2}$, are close to the critical value. It is concluded that fluctuations in scaling rate can lead to breakaway, either through exceeding the alloy's capacity to supply chromium to the scale or by accelerating mechanical failure.

The effect of carbon on the breakaway process is obviously of interest. As already established, the limited carbide precipitation seen beneath Cr_2O_3 does not affect the kinetic stability of the protective scale during steady-state growth, because carbide dissolution releases chromium. During the transient stage following Cr_2O_3 failure, while the demand for chromium is increased, the presence of a carbide plate in the depletion zone may reduce the chromium flux to the alloy surface if carbide dissolution is not instantaneous. However, in most cases examined here, carburisation of the alloy was seen not to be a necessary condition for breakaway. Nevertheless, since the onset of breakaway in CO_2 is greatly accelerated compared with the process in dry air, carbon must play some part in changing scale properties and/or k_{p,Cr_2O_3}.

No direct information is available from the present work for the mechanism of carbon entry into growing chromia scales. It is known [36] that the solubility of carbon in Cr_2O_3 is negligible. In light of this, the observation of carbide formation beneath chromia scales grown on both pure chromium and Fe–Cr alloys led to the proposal [37,38] that carbon penetrated the scales as molecular species (CO/CO_2) along grain boundaries. As scale growth is supported by grain boundary diffusion, alterations to k_{p,Cr_2O_3} can result from direct diffusional interactions, or indirectly from changed grain size and/or shape. In addition, the presence of carbon-bearing species on grain boundaries could affect the scale mechanical properties, rendering it more susceptible to fracture. Information on the form and location of carbon is lacking, and these possibilities cannot be explored further at this time.

4.3 Morphological evolution during breakaway

Fe–20Cr

An early stage of Fe-rich oxide growth on Fe–20Cr is seen in Fig. 3. Beneath the nodule lies a Cr-rich oxide layer which appears to be continuous with the surround-

ing, protective Cr_2O_3 scale. In fact, this layer evidences quite different behaviour at the nodule centre and its periphery. The depletion profile recorded below the outer part of the small nodule, marked by the left hand arrow in Fig. 3a, is shown in Fig. 9e. No significant difference is seen between it and other profiles plotted in the same graph, which were recorded underneath the protective Cr_2O_3 scale, away from any Fe-rich nodule. Thus, the concentration profile is not affected by the presence of the nodule; in particular, the chromium concentration is low below the metal/oxide interface, despite the fact that the outer layer located directly above is pure iron oxide (Fe_2O_3). This apparent contradiction with local mass balance shows that the morphology of the small nodule is transient, of course, and that outward iron diffusion across the metal/oxide interface to form Fe_2O_3 occurred only in the centre of the nodule, at a location where the chromia layer had lost its protective character. Furthermore, internal Cr-rich spinel particles were found below the centre of the nodule, although a Cr_2O_3 layer appeared to be present at the metal surface (# 3 in Fig. 4). Since Cr_2O_3 is inherently more stable than the spinel oxide, local thermodynamic equilibrium along a p_{O_2} gradient would preclude internal spinel precipitation underneath a true Cr_2O_3 layer. This observation also reflects the transient nature of the nodule, and that inward oxygen diffusion to form the internal oxide occurred only beneath the nodule centre, where the Cr-rich layer was no longer protective, and the local oxygen activity had increased.

Halvarsson et al. [39] made very similar observations in a study of 304L steel (18.5 wt. % Cr) oxidation in O_2–H_2O at 600 °C, and their TEM observations coupled with chemical analysis and diffraction studies allowed a more precise characterisation of the oxide phases. Away from the nodules, the protective scale was a Cr-rich corundum type oxide. In regions of breakaway oxidation, the intermediate oxide layer continuous with the protective scale also had a corundum structure, and contained more chromium than the surrounding inner and outer scales. Its chromium content abruptly dropped along the original metal/oxide interface, toward the nodule centre. At the nodule centre, in a 1–2 μm wide region, the chromium content was as low as 40 wt. %, and the oxide had a spinel structure.

The mechanism of breakaway oxidation may then be understood as follows: initially, the alloy surface is covered by a protective Cr_2O_3 scale, which generates a subsurface chromium-depleted zone. Failure of the Cr_2O_3 scale occurs locally, either in a mechanical way such as cracking, or by fluctuations in k_{p,Cr_2O_3}, leading to chemical failure. The chromium-depleted alloy is exposed to the atmosphere and, unable to reform Cr_2O_3, produces spinel oxide. Töpfer et al. [40] showed that the iron tracer diffusion coefficient was about 3 orders of magnitude higher than that of chromium over a range of oxygen activity in $Fe_{3-x}Cr_xO_4$ spinels, with $0 < x < 0.4$, at 1200 °C. This observation is likely to hold, at least qualitatively, at the lower temperature of the present work. Thus, the outward cation flux across the newly formed spinel oxide contains mainly iron, and an outer Fe_2O_3 layer is formed. As a further consequence of spinel formation, the interfacial oxygen activity rises locally, and oxygen permeability reaches a value where outward chromium diffusion from the depleted alloy is not sufficient to prevent internal precipitation of Cr-rich spinel.

At first, the counterflows of iron and oxygen are located in the centre of the nodule, and the nearby alloy is not affected. The processes described above produce a subscale alloy matrix at local equilibrium with the spinel precipitates. Consequently, the interfacial chromium activity is too low to stabilise Cr_2O_3. As oxygen

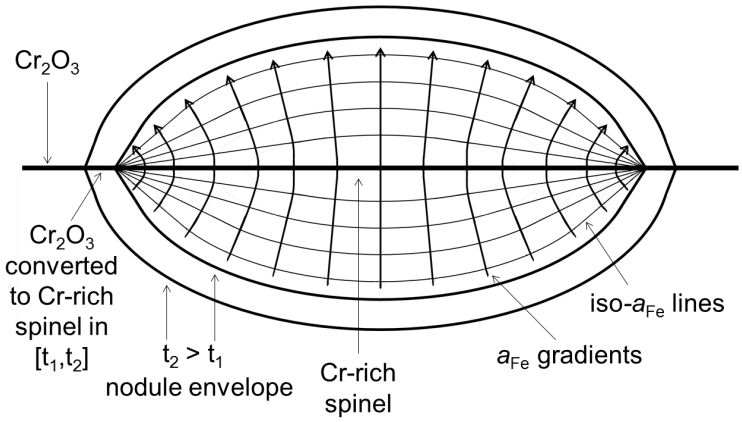

Figure 17: Schematic representation of nodular oxide growth.

diffusion into the alloy is inward but also lateral, internal precipitation and conversion of the Cr_2O_3 layer to spinel oxide spread laterally. Since fast iron and oxygen diffusion across the originally protective layer is limited to a central region, whereas the inner and outer parts may grow in all directions, the nodule assumes an elliptical shape. Then, as oxygen diffuses inward, the depth of the internal oxidation front increases, while the metal matrix surrounding the internal Cr-rich spinel particles is subsequently oxidised into an Fe-rich spinel, forming the two-phase inner oxide layer. Fast outward iron diffusion results in the formation of Fe_3O_4 beneath the first formed Fe_2O_3. Continued nodule growth is proposed to occur by outward iron diffusion along a_{Fe} gradients, which are defined by the iso-a_{Fe} lines, themselves determined by the nodule shape. On this basis, the protective Cr_2O_3 scale is expected to be surrounded by the laterally growing nodule, as shown in Fig. 17. The high iron activity in the outer and inner oxides destabilises Cr_2O_3, which is converted to Cr-rich spinel. A steady-state is thus arrived at, where the elliptical shape is maintained. Describing lateral and vertical growth with the same solid-state diffusion process qualitatively accounts for the fact that lateral growth is parabolic, with a rate proportional to the thickening rate (Fig. 15). Nodule growth and overlapping eventually results in the uniformly thick scales typified by Fig. 6a.

The volume fraction of internal oxides was very high ($f_{V-ox} = 0.7 \pm 0.1$). In particular, it exceeded the value measured by Rapp [41] for the transition from internal to external oxidation of Ag–In alloys at 550 °C, $f^*_{V-ox} = 0.3$. The oxides form such a dense precipitation zone rather than a continuous layer because they are produced by in situ oxidation of preexisting internal carbides [3,42]. Extensive carburisation beneath the Fe-rich oxide nodules and scales causes massive chromium depletion in the alloy matrix, and carbide dissolution cannot sustain the chromium flux required to reform a Cr-rich layer at the base of the scale [2]. Thus whilst internal carburisation is a consequence, not a cause, of the onset of breakaway, subsequent oxidation of the carbides permanently immobilises the chromium, making scale rehealing impossible. Iron-rich oxide formation, together with in situ oxidation of chromium (in the form of internal carbides, internal oxides and Cr-rich oxide particles in the inner scale), are thus maintained in a steady-state of fast reaction.

Fe–20Cr–10Ni and Fe–20Cr–20Ni

Nodules grown on Fe–20Cr–10Ni and Fe–20Cr–20Ni were morphologically similar to those found on Fe–20Cr. The composition of the inner layer was different, as it contained nickel, and internal oxidation was suppressed. A reaction mechanism similar to that discussed above for Fe–20Cr is thought to apply for the 20Cr ternaries. After the protective Cr_2O_3 scale fails and oxygen starts diffusing inward, the most stable spinel $FeCr_2O_4$ is first formed. The surrounding Cr-depleted matrix is then oxidised, producing $NiFe_2O_4$ instead of Fe_3O_4. Since nickel ferrite is inherently less stable than magnetite, as seen from standard free energies [31], its formation reflects a local increase of the Ni/Fe ratio at the metal/oxide interface, relative to the bulk alloy, as a consequence of outward iron diffusion to form the outer oxide layers. This nickel enrichment is, however, too shallow to be detected by SEM-EDS (Fig. 13). Thermodynamic data for the quaternary Fe–Cr–Ni–O system were not available to the present authors, which further hinders a quantitative discussion of the reaction morphology, in particular the absence of internal oxidation.

However, the results can be rationalised qualitatively. No intragranular carbides were formed in the ternary alloys beneath the Fe-rich nodules, probably reflecting the fact that the inner layer, consisting of $FeCr_2O_4$ + $NiFe_2O_4$, was a better barrier to carbon than the Fe-rich + Cr-rich $Fe_{3-x}Cr_xO_4$ mixture formed in Fe–20Cr. A direct comparison of carbon permeability may not be made because the carbon solubility differs between the binary and ternary alloys. Nonetheless, it is clear that the absence of internal carbide in the ternary alloys favoured external over internal oxidation.

The overall nodule growth rate was seen to decrease with alloy nickel concentration (Table 2). The explanation was provided by Croll and Wallwork [43], who showed that reduced rates were due to nickel enrichment in the scale, and to the fact that $NiFe_2O_4$ was a slower cation diffuser than the nickel deficient $Ni_xFe_{3-x}O_4$.

Fe–25Cr

Failure of the protective Cr_2O_3 scale on the Fe–25Cr alloy resulted in two types of oxides: thick Fe-rich nodules near the edges of the specimens, and "healed scale" on the specimen faces, containing a Cr-rich inner layer, of either spinel or corundum type. Whittle and Wood [20] reported similar scale morphologies after breakaway of an Fe–18Cr alloy at 800–1200 °C in air. Near the specimen edges, the high surface to volume ratio, and/or significant spallation, results in severe chromium depletion and formation of the Fe-rich scale, with a mechanism similar to that proposed for Fe–20Cr. Away from the edges, the chromium concentration at the Cr_2O_3/alloy interface is quite high (10–15 at. % as determined from Eq. (3)) and enables the formation of a Cr-rich oxide after localised failure of Cr_2O_3. At low p_{O_2}, the diffusion coefficient of both iron and chromium decreases with increasing chromium content in the Fe–Cr spinel oxide [40]. The formation of a Cr-rich, "healing" layer at the base of the scale, accounts for the low scaling rate, as compared to that of the Fe-rich thick nodules. Furthermore, the healed scale was seen to be a relatively good barrier to carbon, preventing carburisation (Fig. 11a). Thus, chromium diffusion in the alloy toward the metal/oxide interface is not hindered, and the relatively protective morphology is maintained.

Fe–25Cr–10Ni and Fe–25Cr–20Ni

Although the 25Cr ternary alloys formed some oxide nodules in addition to Cr_2O_3, their size and surface coverage were much lower than for the other alloys. The constitution of these nodules was not studied, as none were seen in the cross-sections prepared. Nonetheless, as separate additions of chromium or nickel to the Fe–20Cr alloy each resulted in slower scale growth, it may be assumed that simultaneous additions of both caused further reductions in the growth rate, so that nodule development was drastically limited.

4.4 Influence of water vapour

Additions of H_2O (g) had no significant effect on the extent of nodule formation on Fe–20Cr–10Ni and Fe–20Cr–20Ni, but accelerated the onset of breakaway oxidation for the binary alloys. Chromia scales are known [9–12] to grow faster in the presence of H_2O (g), but this could not be verified in the present work, as differences in Cr_2O_3 scale thickness between dry and wet CO_2 were not more important than local variations on a given specimen.

Water vapour had no significant effect on carburisation of the Fe–20Cr alloy. However, in the case of Fe–25Cr and Fe–20Cr–10Ni, the extent of carbide precipitation was decreased by H_2O (g) additions. All types of carburisation morphology were affected: intergranular precipitation, formation of plate-like carbides beneath Cr_2O_3 and extensive precipitation beneath iron-rich nodules and scales. A reduced carburisation rate in the presence of H_2O (g) was reported earlier [24] for an Fe–9Cr alloy reacted in dry and wet CO_2 at 650 °C. The effect of H_2O (g) was interpreted in terms of preferential uptake and/or transport of H-bearing molecules over C-bearing species.

Since carburisation was reduced by H_2O (g), the reason for accelerated breakaway in wet CO_2 appears to be unrelated to carbide precipitation. Analysis of nodule development kinetics is needed in order to gain insight into the influence of H_2O on breakaway oxidation; this is addressed in a companion paper [22].

5 Conclusions

All alloys developed Cr_2O_3 scales in both dry and wet CO_2 mixtures, but long term (336 h) protection was achieved only in the case of Fe–25Cr–10,20Ni ternaries. Breakaway oxidation of Fe–20Cr, Fe–20Cr–10Ni, Fe–20Cr–20Ni and Fe–25Cr resulted from the nucleation and growth of iron-rich nodules. Higher chromium levels sometimes permit formation beneath the nodules of a healing oxide layer relatively rich in chromium, which slows the local corrosion rate. Nickel additions lead to formation of $NiFe_2O_4$ in the nodule inner layers, where this phase acts as a block to diffusion, also slowing reaction.

Carburisation observed beneath large nodules on the ferritic alloys is a consequence, and not a cause, of iron-rich oxide growth. The increase in carbon uptake is attributed to a carbon permeability which is greater in the iron-rich oxide than in the chromia it replaces.

Chromia scale growth is accompanied by alloy subscale depletion in chromium. Measured chromium concentration profiles reflect the diffusional properties of the

alloy, and are unaffected by the presence in the depletion zone of limited amounts of chromium-rich carbide. Interfacial chromium concentration values, N^i_{Cr}, are in agreement with predictions of Wagner's theory, confirming the establishment of a kinetic steady state.

Fluctuations in local chromia scaling rate are reflected in varying scale thickness and values of N^i_{Cr}. These fluctuations can lead to breakaway, either through exceeding the alloy's capacity to supply chromium, or by accelerating mechanical failure of the scale. Subsequent increases in the oxygen activity at the alloy-oxide interface lead to outward diffusion of iron to form iron oxide, and conversion of the chromia to spinel. These changes spread laterally from the initiation site.

Carbon accelerates the onset of breakaway compared with the situation in dry air. This effect is attributed to carbon entry into the chromia scale, probably along its grain boundaries, where it can affect grain growth, boundary diffusion and scale mechanical properties.

Acknowledgements

Financial support from the Australian Research Council Discovery program is gratefully acknowledged.

References

[1] S. Sridhar, P. Rozzelle, B. Morreale and D. Alman, Materials challenges for advanced combustion and gasification fossil energy systems, Metallurgical and Materials Transactions A 42 (2011) pp. 871–877. doi: 10.1007/s11661-011-0627-x.

[2] C. S. Giggins and F. S. Pettit, Corrosion of metals and alloys in mixed gas environments at elevated temperatures, Oxidation of Metals 14 (1980) pp. 363–413. doi: 10.1007/BF00603609.

[3] J. Pirón Abellán, T. Olszewski, H. Penkalla, G. Meier, L. Singheiser and W. Quadakkers, Scale formation mechanisms of martensitic steels in high CO_2/H_2O-containing gases simulating oxyfuel environments, Materials at High Temperatures 26 (2009) pp. 63–72. doi: 10.3184/096034009X438185.

[4] G. H. Meier, K. Jung, N. Mu, N. M. Yanar, F. S. Pettit, J. Pirón Abellán, T. Olszewski, L. Nieto Hierro, W. J. Quadakkers and G. R. Holcomb, Effect of alloy composition and exposure conditions on the selective oxidation behavior of ferritic Fe–Cr and Fe–Cr–X alloys, Oxidation of Metals 74 (2010) pp. 319–340. doi: 10.1007/s11085-010-9215-5.

[5] I. Kvernes, M. Oliveira and P. Kofstad, High temperature oxidation of Fe–13Cr–xAl alloys in air–H_2O vapour mixtures, Corrosion Science 17 (1977) pp. 237–252. doi: 10.1016/0010-938X(77)90049-X.

[6] Y. Ikeda and K. Nii, Mechanism of accelerated oxidation of Fe–Cr alloys in water vapor containing atmosphere, Transactions of National Research Institute for Metals 26 (1984) pp. 52–62.

[7] S. Henry, A. Galerie and L. Antoni, Abnormal oxidation of stabilized ferritic stainless steels in water vapor, Materials Science Forum 369–372 (2001) pp. 353–360. doi: 10.4028/www.scientific.net/MSF.369-372.353.

[8] J. Ehlers, D. Young, E. Smaardijk, A. Tyagi, H. Penkalla, L. Singheiser and W. Quadakkers, Enhanced oxidation of the 9%Cr steel P91 in water vapour containing environments, Corrosion Science 48 (2006) pp. 3428–3454. doi: 10.1016/j.corsci.2006.02.002.

[9] N. K. Othman, J. Zhang and D. J. Young, Water vapour effects on Fe–Cr alloy oxidation, Oxidation of Metals 73 (2010) pp. 337–352. doi: 10.1007/s11085-009-9183-9.

[10] G. Hultquist, B. Tveten and E. Hörnlund, Hydrogen in chromium: Influence on the high-temperature oxidation kinetics in H_2O, oxide-growth mechanisms, and scale adherence, Oxidation of Metals 54 (2000) pp. 1–10. doi: 10.1023/A:1004610626903.

[11] S. Henry, J. Mougin, Y. Wouters, J.-P. Petit and A. Galerie, Characterization of chromia scales grown on pure chromium in different oxidizing atmospheres, Materials at High Temperatures 17 (2000) pp. 231–234. doi: 10.1179/mht.2000.17.2.008.

[12] M. Michalik, M. Hänsel, J. Zurek, L. Singheiser and W. Quadakkers, Effect of water vapour on growth and adherence of chromia scales formed on Cr in high and low p_{O_2}-environments at 1000 and 1050 °C, Materials at High Temperatures 22 (2005) pp. 213–221. doi: 10.1179/mht.2005.025.

[13] A. Galerie, Y. Wouters and M. Caillet, The kinetic behaviour of metals in water vapour at high temperatures: Can general rules be proposed?, Materials Science Forum 369–372 (2001) pp. 231–238. doi: 10.4028/www.scientific.net/MSF.369-372.231.

[14] E. Essuman, G. H. Meier, J. Żurek, M. Hänsel and W. J. Quadakkers, The effect of water vapor on selective oxidation of Fe–Cr alloys, Oxidation of Metals 69 (2008) pp. 143–162. doi: 10.1007/s11085-007-9090-x.

[15] H. Asteman, J.-E. Svensson, L.-G. Johansson and M. Norell, Indication of chromium oxide hydroxide evaporation during oxidation of 304L at 873 K in the presence of 10% water vapor, Oxidation of Metals 52 (1999) pp. 95–111. doi: 10.1023/A:1018875024306.

[16] H. Asteman, J.-E. Svensson, M. Norell and L.-G. Johansson, Influence of water vapor and flow rate on the high-temperature oxidation of 304L; effect of chromium oxide hydroxide evaporation, Oxidation of Metals 54 (2000) pp. 11–26. doi: 10.1023/A:1004642310974.

[17] D. Whittle, G. Wood, D. Evans and D. Scully, Concentration profiles in the underlying alloy during the oxidation of iron-chromium alloys, Acta Metallurgica 15 (1967) pp. 1747–1755. doi: 10.1016/0001-6160(67)90066-1.

[18] H. E. Evans, A. T. Donaldson and T. C. Gilmour, Mechanisms of breakaway oxidation and application to a chromia-forming steel, Oxidation of Metals 52 (1999) pp. 379–402. doi: 10.1023/A:1018855914737.

[19] G. Wood and D. Whittle, The mechanism of breakthrough of protective chromium oxide scales on Fe–Cr alloys, Corrosion Science 7 (1967) pp. 763–782. doi: 10.1016/S0010-938X(67)80003-9.

[20] D. P. Whittle and G. C. Wood, Complex scale formation on an iron-18% chromium alloy, Journal of The Electrochemical Society 114 (1967) pp. 986–993. doi: 10.1149/1.2424198.

[21] K. McCarty and D. Boehme, A raman study of the systems $Fe_{3-x}Cr_xO_4$ and $Fe_{2-x}Cr_xO_3$, Journal of Solid State Chemistry 79 (1989) pp. 19–27. doi: 10.1016/0022-4596(89)90245-4.

[22] T. Gheno, D. Monceau and D. J. Young, Kinetics of breakaway oxidation of Fe–Cr and Fe–Cr–Ni alloys in dry and wet carbon dioxide, Corrosion Science 77 (2013) pp. 246–256. doi: 10.1016/j.corsci.2013.08.008.

[23] H. Davies and A. Dinsdale, Theoretical study of steam grown oxides as a function of temperature, pressure and p(o2), Materials at High Temperatures 22 (2005) pp. 15–25. doi: 10.1179/mht.2005.003.

[24] T. Gheno, D. Monceau, J. Zhang and D. J. Young, Carburisation of ferritic Fe–Cr alloys by low carbon activity gases, Corrosion Science 53 (2011) pp. 2767–2777. doi: 10.1016/j.corsci.2011.05.013.

[25] M. da Cunha Belo, M. Walls, N. Hakiki, J. Corset, E. Picquenard, G. Sagon and D. Noël, Composition, structure and properties of the oxide films formed on the stainless steel 316L in a primary type PWR environment, Corrosion Science 40 (1998) pp. 447–463. doi: 10.1016/S0010-938X(97)00158-3.

[26] C. Wagner, Theoretical analysis of the diffusion processes determining the oxidation rate of alloys, Journal of the Electrochemical Society 99 (1952) pp. 369–380. doi: 10.1149/1.2779605.

[27] A. W. Bowen and G. M. Leak, Solute diffusion in alpha- and gamma-iron, Metallurgical Transactions 1 (1970) pp. 1695–1700. doi: 10.1007/BF02642019.

[28] J. Crank, *The Mathematics of Diffusion.* Oxford University Press, Oxford, 2nd ed. (1975).

[29] P. Kofstad, *High temperature corrosion.* Elsevier Applied Science Publishers (1988).

[30] B. Sundman, B. Jansson and J. O. Andersson, The Thermo-Calc databank system, Calphad 9 (1985) pp. 153–190. doi: 10.1016/0364-5916(85)90021-5.

[31] I. Barin, *Thermochemical Data of Pure Substances.* VCH second ed. (1993).

[32] O. Kubaschewski and C. Alcock, *Metallurgical Thermochemistry.* Pergamon Press, Oxford, 5th ed. (1979).

[33] D. J. Young, *High Temperature Oxidation and Corrosion of Metals.* Elsevier Corrosion Series Elsevier (2008).

[34] R. A. Holm and H. E. Evans, The resistance of 20Cr/25Ni steels to carbon deposition. III. Cold work and selective pre-oxidation, Materials and Corrosion 38 (1987) pp. 219–224. doi: 10.1002/maco.19870380502.

[35] D. P. Whittle, Spalling of protective oxide scales, Oxidation of Metals 4 (1972) pp. 171–179. doi: 10.1007/BF00613091.

[36] I. Wolf and H. Grabke, A study on the solubility and distribution of carbon in oxides, Solid State Communications 54 (1985) pp. 5–10. doi: 10.1016/0038-1098(85)91021-X.

[37] X. G. Zheng and D. J. Young, High-temperature corrosion of Cr_2O_3-forming alloys in CO–CO_2–N_2 atmospheres, Oxidation of Metals 42 (1994) pp. 163–190. doi: 10.1007/BF01052021.

[38] X. Zheng and D. Young, High temperature corrosion of pure chromium in CO–CO_2–SO_2–N_2 atmospheres, Corrosion Science 36 (1994) pp. 1999–2015. doi: 10.1016/0010-938X(94)90004-3.

[39] M. Halvarsson, J. Tang, H. Asteman, J.-E. Svensson and L.-G. Johansson, Microstructural investigation of the breakdown of the protective oxide scale on a 304 steel in the presence of oxygen and water vapour at 600 °C, Corrosion Science 48 (2006) pp. 2014–2035. doi: 10.1016/j.corsci.2005.08.012.

[40] J. Töpfer, S. Aggarwal and R. Dieckmann, Point defects and cation tracer diffusion in $(Cr_xFe_{1-x})_{3-\delta}O_4$ spinels, Solid State Ionics 81 (1995) pp. 251–266. doi: 10.1016/0167-2738(95)00190-H.

[41] R. Rapp, The transition from internal to external oxidation and the formation of interruption bands in silver-indium alloys, Acta Metallurgica 9 (1961) pp. 730–741. doi: 10.1016/0001-6160(61)90103-1.

[42] C. T. Fujii and R. A. Meussner, Carburization of Fe–Cr alloys during oxidation in dry carbon dioxide, Journal of the Electrochemical Society 114 (1967) pp. 435–442. doi: 10.1149/1.2426622.

[43] J. E. Croll and G. R. Wallwork, The high-temperature oxidation of iron-chromium-nickel alloys containing 0–30% chromium, Oxidation of Metals 4 (1972) pp. 121–140. doi: 10.1007/BF00613088.